Hindawi
Mathematical Problems in Engineering
Volume 2019, Article ID 8370827, 20 pages
https://doi.org/10.1155/2019/8370827

Research Article

Dynamics Modeling and Analysis of a Novel Constraint Metamorphic Reversible Plough

Yanyan Song,[1,2] Boyan Chang,[1,2] Guoguang Jin,[1,2] Zhan Wei,[1,2] and Bo Li[1,2]

[1]*School of Mechanical Engineering, Tianjin Polytechnic University, Tianjin 300387, China*
[2]*Tianjin Key Laboratory of Advanced Mechatronics Equipment Technology, Tianjin 300387, China*

Correspondence should be addressed to Guoguang Jin; jinguoguang@tjpu.edu.cn

Received 24 June 2019; Revised 17 August 2019; Accepted 31 August 2019; Published 22 September 2019

Academic Editor: Roberto Fedele

To meet the requirements of different farming objects, this paper presents a novel constraint metamorphic reversible plough (CMRP) which has four distinct working phases and the feature of underactuation, and its prototype has been manufactured for practical testing purposes. Firstly, the kinematics of the mechanism in each phase are studied systematically with the closed-loop vector method, including displacement, velocity, and acceleration analysis. Considering the underactuated characteristics of the mechanism in the source phase, its dynamic models in the source phase are further established by the Lagrange equation. Based on the theory that velocity and acceleration are the same in an extremely brief period, the motion laws of the slider in the source phase can be obtained. To obtain the constraint force/torque acting on the crucial joints in each phase, the dynamic model of the CMRP is established by the Newton–Euler equation. Furthermore, the initial position of the CMRP with a flexible prismatic joint can be determined using the static balance equation. Finally, the obtained kinematic and dynamic models of the CMRP in each phase are verified, respectively, through comparing the simulation results in SolidWorks and Matlab software, and the experiment with the prototype is conducted. The CMRP proposed in this study provides a feasible technical scheme for improving the capability of reversible plough over unknown and complex terrains.

1. Introduction

The two-way plough can perform two-way tillage, which is a plough for the tractor ploughing unit to perform one-way tillage in one round trip, and it can be divided into the reversible plough [1, 2] and the horizontally reversible plough [3]. The rotary plough frames of the reversible plough are equipped with two sets of plough bodies, and the two sets of plough bodies are alternately operated in the round trip by the reversible mechanism; the unidirectional turning is realized while having better tumbling coverage performance [4]. To date, many scholars have carried out thorough research into the reversible plough. Gebresenbet et al. [5] designed and developed a reversible animal-drawn plough, which is developed on the basis of laboratory experiments reported earlier to determine optimum parameters for a curved implement. Moitzi et al. [6] studied the influence of working width of reversible plough and T-trailed cultivator on field capacity, fuel consumption, slip, and specific energy consumption. Mahmoodi et al. [7] identified a way to use a mathematical approach for the design of a moldboard plough. Comparing the determined guide curve extracted from this approach with traditional methods revealed that this approach not only can be a useful tool to design the moldboard plough with different curvatures but also can relatively easily determine the guide curve for the moldboard plough, which is traditionally considered as a very tedious and time-consuming task. With the rapid development of agricultural mechanization, the reversible plough with changeable structures and mobility is expected in production to accommodate different operation environments and meet various task requirements. Several kinds of mechanisms such as the kinematotropic linkages [8] and metamorphic mechanisms [9, 10] have been developed in the past decades.

Metamorphic mechanisms are a new kind of mechanism originated from the configuration and mobility researches of decorative carton folds. Compared with traditional mechanisms, metamorphic mechanisms have the advantages of multifunctional stages, multitopological structures, and multidegree of freedom [11]. Meanwhile, according to the functional requirements or changes in the environment, metamorphic mechanisms can adapt to different tasks and be flexibly applied to different occasions by changing its configuration in motion and self-restructuring or reconstruction. It is well known that the constraint metamorphic mechanism is a metamorphic mechanism that constrains movement cycles of metamorphic joints and is commonly used in practical operation, which is easy to control and realize [12]. Li et al. [13] proposed a method for designing the configuration of constraint metamorphic mechanisms according to the task requirements, which include the types of metamorphic kinematic pairs and the ways of constraints. Xu et al. [14] designed a metamorphic mechanism cell, which can realize deploying, self-locking, unlocking, retracting, and interlocking with other cells, by incorporating the variable kinematic joints. Ma et al. [15] presented two novel 6R metamorphic linkages as the spherical-planar metamorphic linkage and the Bennett-spherical metamorphic linkage with each of them having three motion branches. And they analyzed the reconfiguration of both linkages and revealed the geometrical constraints for motion branch transformations.

Above all, the principle of constraint metamorphosis is applied to the reversible plough, and a novel CMRP is designed. The CMRP not only has the characteristics of controllable, adjustable, and output performance of the controllable mechanism but also has the characteristics of multifunctional stages, multitopological structures, and multidegree of freedom of constraint metamorphic mechanism, which makes the CMRP flexibly applied to different occasions and different working objects.

Kinematic analysis [16] can reflect the kinematic characteristics of mechanisms, so it is very important for the CMRP. For example, kinematic models are essential for trajectory planning, computer simulation, and real-time control. Kinematic models are also the basis of dynamic models. More importantly, dynamic models contribute to the dynamic analysis and synthesis and are the basis of high precision in real control. For example, the analytical results of a dynamic model can be used for simulations, actuator selection, mechanical vibration analysis, and dynamic optimization.

Popular dynamic model methods include the Lagrange equation [17, 18], the Newton–Euler method [19], the Kane equation [20], the D'Alembert method [21], and the virtual work principle [22]. Gan et al. [23] presented a unified inverse kinematic and dynamic model of a metamorphic parallel mechanism with pure rotation and pure translation phases by using the Newton–Euler method. Jin et al. [24, 25] established dynamic equations of the metamorphic mechanism for an arbitrary configuration according to Kane's equations. From these literatures, we know that the Lagrange equation needs to get the kinetic energy and potential energy of each part of the constraint metamorphic mechanism; the Newton–Euler method and Kane method involve differential equation causing the increase of calculated amount; the D'Alembert method states that the sum of the external forces, inertia forces, and joint forces is zero; the virtual work principle is known as the work of a force on a particle along a virtual displacement. So the appropriate solving method used in dynamics modeling is quite important. On the contrary, they are associated with the risk of errors. Selecting correct methods to improve gross performances and establishing the basic kinematic and dynamic models are all essential to design a novel CMRP which can be successfully used in agriculture.

In this paper, the principle of constraint metamorphosis is introduced into the design of the reversible plough, and a novel CMRP is designed. By using the Lagrange equation, the dynamics in the source phase are analyzed. Based on the theory that velocity and acceleration is the same in an extremely brief period, the motion law of the slider in the source phase can be obtained. Moreover, the dynamic model of the CMRP in each phase is established by the Newton–Euler equation. The dynamic performance of the CMRP such as the driving forces and the constraint forces/torques acting on the crucial joints will be analyzed in each phase, which provides a theoretical foundation for further study.

2. Structure Description and Kinematic Analysis

2.1. Structure Description. Figure 1 shows the computer aided design (SolidWorks) model of the CMRP, which is composed by a frame, a rotary plough frame, a slider, a compatibility rod, two springs, and two hydraulic cylinders. In addition, the frame is welded with baffles to limit the position of the rotary plough frame.

The schematic diagram of the CMRP is shown in Figure 2, in which the cylinders 5 and 7 of the two hydraulic cylinders and the frame 0 are hinged at joints D and E, and the corresponding cylinder rods 4 and 6 and the compatibility rod 2 are hinged at joints B and C, respectively. The compatibility rod 2 and the slider 3 are hinged at joint A, and the slider 3 is connected to the rotary plough frame 1 by two springs. At this time, the prismatic joint P_3 between the slider 3 and the rotary plough frame 1 can be treated as a flexible prismatic joint. The rotary plough frame 1 and the frame 0 are hinged at joint O, resulting a closed kinematic chain. The system drives the rotary plough frame 1 to perform a 180-degree reciprocating inversion through the joint action of the two hydraulic cylinders which can realize the alternate operation of the CMRP in the round trip.

Different from the horizontally reversible plough proposed in reference [26], the CMRP presented in this paper has four distinct working phases. As shown in Figure 3, the four distinct working phases of the CMRP can be expressed as follows.

Configuration 1. As shown in Figure 3(a), the degrees of freedom (DOFs) of the mechanism in the source

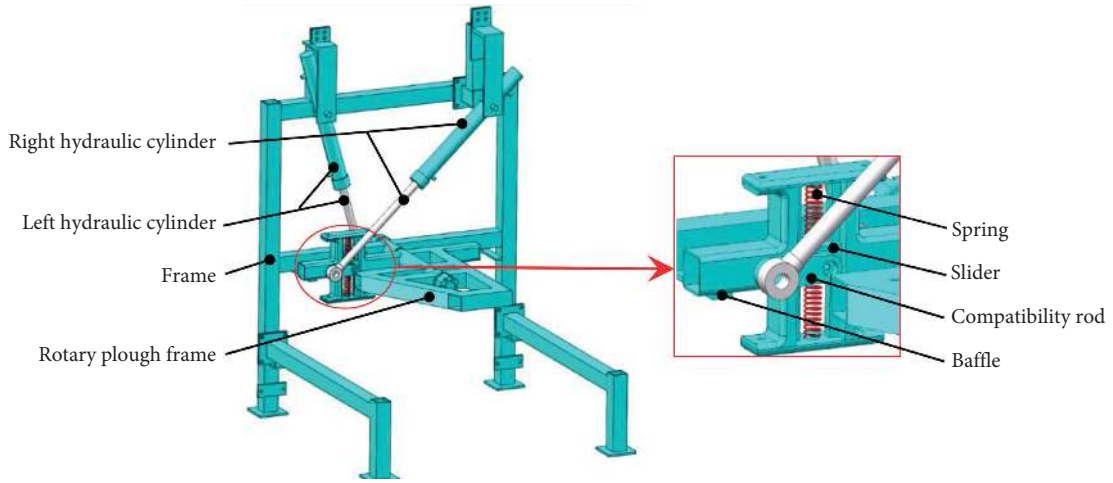

Figure 1: The computer aided design (SolidWorks) model of the CMRP.

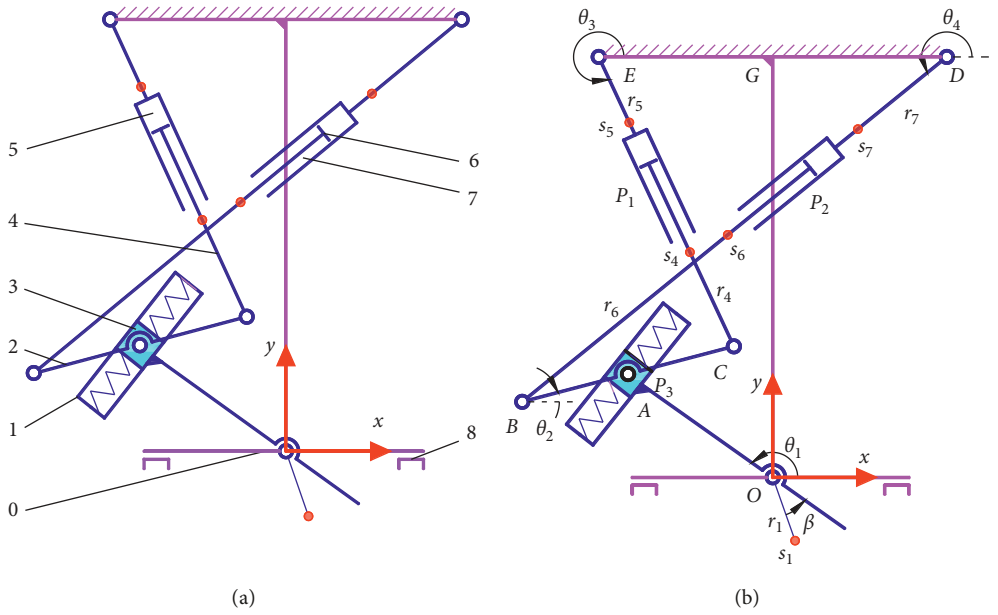

(a) (b)

Figure 2: (a) Composition and (b) schematic diagrams of the CMRP. 0, frame; 1, rotary plough frame; 2, compatibility rod; 3, slider; 4, left cylinder rod; 5, left hydraulic cylinder; 6, right cylinder rod; 7, right hydraulic cylinder; 8, baffle.

phase can be obtained using the Grübler–Kutzbach criterion as follows:

$$F = \sum_{i=1}^{m} f_i - d(m - n + 1) = 9 - 3(9 - 8 + 1) = 3, \quad (1)$$

where F is the DOFs of the mechanism; f_i is the DOFs of the ith kinematic joint; d is the order of the mechanism, and $d = 6 - \lambda$; λ is the public constraints; m is the number of components including frame; and n is the number of kinematic joints.

In the source phase, the mechanism can be regarded as an equivalent eight-bar planar linkage which has six revolute joints O, A, B, C, D, and E and three prismatic joints P_1, P_2, and P_3, and the number of actuators of the mechanism is less than the number of DOF; therefore, the mechanism in the source phase is an underactuated mechanism.

Configuration 2. In this configuration, the metamorphosis of the mechanism is mainly realized by geometric constraint offered by the baffle when the rotary plough frame rotates to the phase in Figure 3(b). There is no relative movement between the rotary plough frame and the frame. According to the Grübler–Kutzbach criterion, the DOFs of the mechanism can be obtained as follows:

$$F = \sum_{i=1}^{m} f_i - d(m - n + 1) = 8 - 3(8 - 7 + 1) = 2. \quad (2)$$

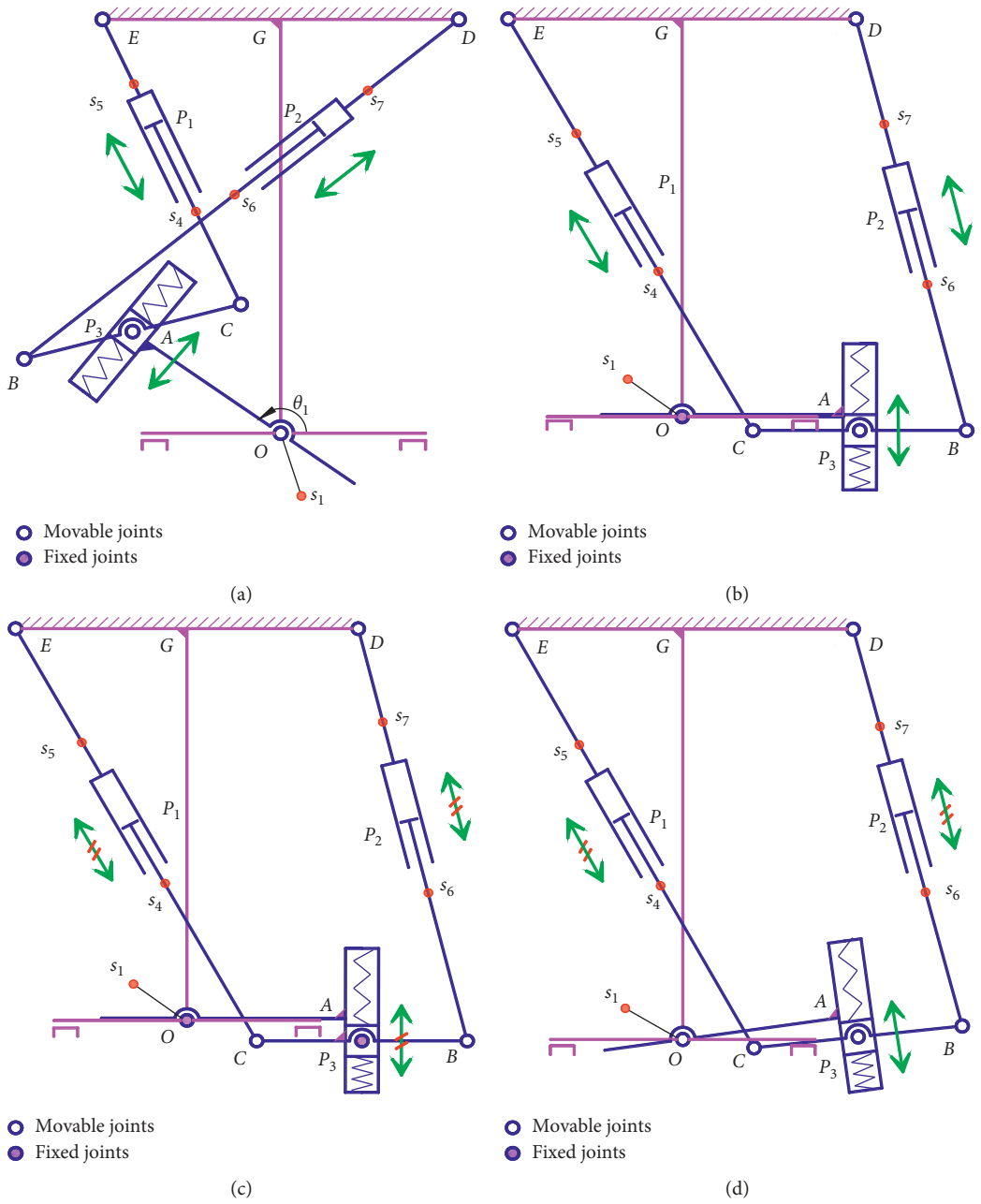

Figure 3: Equivalent mechanisms of the CMRP in different stages: (a) source phase, (b) adjustment phase, (c) normal working phase, and (d) special phase of equivalent mechanism.

Now, the mechanism works as an equivalent seven-bar planar linkage with five revolute joints A, B, C, D, and E and three prismatic joints P_1, P_2, and P_3, and two hydraulic cylinders fully actuate the mechanism. In this working phase, the mechanism can adapt to soil with a different hardness by adjusting the deformation of springs; therefore, this working phase can be denoted with the adjustment phase.

Configuration 3. When the deformation of springs reaches a certain position shown in Figure 3(c), the revolute joints O and A and the prismatic joint P_3 can be, respectively, seen as a fixed joint, and the DOFs of the mechanism can be obtained using the Grübler-Kutzbach criterion as follows:

$$F = \sum_{i=1}^{m} f_i - d(m - n + 1) = 6 - 3(6 - 5 + 1) = 0. \quad (3)$$

In this time, the mechanism is in static balance and the rotary plough frame no longer rotates. In addition, the system state variables of the mechanism are consistent with the system state variables at the end of the

adjustment phase. This working phase can be denoted with the normal working phase.

Configuration 4. The metamorphosis of the mechanism is mainly realized by force constraint. When the mechanism moves to the phase in Figure 3(d), the rotary plough frame is disturbed by uncertainties such as stones and exceptionally hard soil, which is unavoidable in the process of cultivation. To avoid the damage of the plough blade, the mechanism will move in the way in Figure 3(d). And the prismatic joints P_1 and P_2 can be, respectively, seen as a fixed joint. In addition, the DOFs of the mechanism can be obtained using the Grübler-Kutzbach criterion as follows:

$$F = \sum_{i=1}^{m} f_i - d(m - n + 1) = 7 - 3(7 - 6 + 1) = 1. \quad (4)$$

At this time, the rotary plough frame is driven by an external force, and the mechanism works as an equivalent six-bar planar linkage with six revolute joints O, A, B, C, D, and E and a prismatic joint P_3. This working phase can be denoted with special phase.

In summary, the CMRP has four phases including the source phase, the adjustment phase, the normal working phase, and the special phase. The source phase is a transferring phase, and the adjustment phase, the normal working phase, and the special phase can return to the source phase by releasing the constraints at the revolute joints and prismatic joints.

2.2. Displacement Analysis. The kinematic characteristics of the CMRP in each working phase are analyzed based on the closed-loop vector method. For convenience of the following analysis, a coordinate system is established in Figure 2. With reference frame $\{O\}$, O-xy is attached to the frame.

2.2.1. Displacement Analysis of the Source Phase. As shown in Figure 2, θ_1, θ_2, θ_3, and θ_4 are the angle between the rotary plough frame, the compatibility rod, the cylinders of the two hydraulic cylinders, and the x-axis, respectively. $L_{OA'}$, $L_{A'A}$, L_{AB}, L_{BD}, L_{GD}, L_{OG}, L_{GE}, L_{CE}, and L_{AC} represent the length of the line segment corresponding to two points, respectively. To simplify the annotation, A' is not shown in Figure 2, and A' represents the central position of the slider track.

For the closed-loop kinematic chain $OA'ABDGO$, the closed-loop vector equation can be written as follows:

$$\begin{cases} L_{OA'}\cos\theta_1 - L_{A'A}\sin\theta_1 - L_{AB}\cos\theta_2 - L_{BD}\cos\theta_4 = L_{GD}, \\ L_{OA'}\sin\theta_1 + L_{A'A}\cos\theta_1 - L_{AB}\sin\theta_2 - L_{BD}\sin\theta_4 = L_{OG}. \end{cases} \quad (5)$$

For the closed-loop kinematic chain $OA'ACEGO$, the closed-loop vector equation can be written as follows:

$$\begin{cases} L_{OA'}\cos\theta_1 - L_{A'A}\sin\theta_1 + L_{AC}\cos\theta_2 - L_{CE}\cos\theta_3 = -L_{GE}, \\ L_{OA'}\sin\theta_1 + L_{A'A}\cos\theta_1 + L_{AC}\sin\theta_2 - L_{CE}\sin\theta_3 = L_{OG}. \end{cases} \quad (6)$$

θ_3, θ_4, L_{BD}, and L_{CE} can be obtained according to equations (5) and (6), respectively, and expressed as

$$\theta_3 = \arctan\left(\frac{L_{OA'}\sin\theta_1 + L_{A'A}\cos\theta_1 + L_{AC}\sin\theta_2 - L_{OG}}{L_{OA'}\cos\theta_1 - L_{A'A}\sin\theta_1 + L_{AC}\cos\theta_2 + L_{GE}}\right), \quad (7)$$

$$\theta_4 = \arctan\left(\frac{L_{OA'}\sin\theta_1 + L_{A'A}\cos\theta_1 - L_{AB}\sin\theta_2 - L_{OG}}{L_{OA'}\cos\theta_1 - L_{A'A}\sin\theta_1 - L_{AB}\cos\theta_2 - L_{GD}}\right), \quad (8)$$

$$L_{BD} = \sqrt{\left(L_{OA'}\sin\theta_1 + L_{A'A}\cos\theta_1 - L_{AB}\sin\theta_2 - L_{OG}\right)^2 + \left(L_{OA'}\cos\theta_1 - L_{A'A}\sin\theta_1 - L_{AB}\cos\theta_2 - L_{GD}\right)^2}, \quad (9)$$

$$L_{CE} = \sqrt{\left(L_{OA'}\sin\theta_1 + L_{A'A}\cos\theta_1 + L_{AC}\sin\theta_2 - L_{OG}\right)^2 + \left(L_{OA'}\cos\theta_1 - L_{A'A}\sin\theta_1 + L_{AC}\cos\theta_2 + L_{GE}\right)^2}. \quad (10)$$

The number of actuators of the CMRP is less than the DOF in the source phase, which is an underactuated mechanism. For such mechanism, both kinematic analysis and dynamic analysis must be performed. This issue will be explained in detail in Section 3.1.

2.2.2. Displacement Analysis of the Adjustment Phase. As shown in Figure 3(b), by substituting $\theta_1 = 0$, $\theta_2 = 0$, and $L_{A'A} = 0.015\sin(0.25\pi t)$ into equations (7)–(10), θ_3, θ_4, L_{BD}, and L_{CE} in the adjustment phase can be obtained, respectively.

2.2.3. Displacement Analysis of the Normal Working Phase. As shown in Figure 3(c), in the normal working phase, the two hydraulic cylinders are locked and the springs are in an equilibrium position, at which time the arable work can be performed. The values of θ_3, θ_4, L_{BD}, and L_{CE} are the same as the values at the end of the adjustment phase.

2.2.4. Displacement Analysis of the Special Phase. For the CMRP, as mentioned above, the two hydraulic cylinders are not operated during the special phase. Thus, the closed-loop

vector equations in the kinematic diagram, as shown in Figure 3(d), can be written as follows:

$$L_{OA'}\cos\theta_1 + L_{A'A}\sin\theta_1 - L_{AB}\cos\theta_2 - L_{BD}\cos\theta_4 - L_{GD} = 0, \tag{11}$$

$$L_{OA'}\sin\theta_1 - L_{A'A}\cos\theta_1 - L_{AB}\sin\theta_2 - L_{BD}\sin\theta_4 - L_{OG} = 0, \tag{12}$$

$$L_{OA'}\cos\theta_1 + L_{A'A}\sin\theta_1 + L_{AC}\cos\theta_2 - L_{CE}\cos\theta_3 - L_{GE} = 0, \tag{13}$$

$$L_{OA'}\sin\theta_1 - L_{A'A}\cos\theta_1 + L_{AC}\sin\theta_2 - L_{CE}\sin\theta_3 - L_{OG} = 0. \tag{14}$$

The above equations are a set of highly nonlinear equations. Therefore, it cannot be solved directly and solved by the Newton–Raphson algorithm [27, 28]. The purpose of the Newton–Raphson method is to calculate a local solution of the forward kinematic problem based on the iterative procedure and an initial guessing. It is known to list the matrix equations for solving unknowns' increments according to the Newton–Raphson algorithm as follows:

$$\begin{pmatrix} \sin\theta_1 & L_{AB}\sin\theta_2 & 0 & L_{BD}\sin\theta_4 \\ -\cos\theta_1 & -L_{AB}\cos\theta_2 & 0 & -L_{BD}\cos\theta_4 \\ \sin\theta_1 & -L_{AC}\sin\theta_2 & L_{CE}\sin\theta_3 & 0 \\ -\cos\theta_1 & L_{AC}\cos\theta_2 & -L_{CE}\cos\theta_3 & 0 \end{pmatrix} \begin{pmatrix} \Delta L_{A'A} \\ \Delta\theta_2 \\ \Delta\theta_3 \\ \Delta\theta_4 \end{pmatrix} = \begin{pmatrix} -f_1 \\ -f_2 \\ -f_3 \\ -f_4 \end{pmatrix}, \tag{15}$$

in which

$$\begin{aligned} f_1 &= -L_{OA'}\dot{\theta}_1\sin\theta_1 + L_{A'A}\dot{\theta}_1\cos\theta_1, \\ f_2 &= L_{OA'}\dot{\theta}_1\cos\theta_1 + L_{A'A}\dot{\theta}_1\sin\theta_1, \\ f_3 &= f_1, \\ f_4 &= f_2. \end{aligned} \tag{16}$$

A set of initial values $L_{A'A}^{(0)}$, $\theta_2^{(0)}$, $\theta_3^{(0)}$, and $\theta_4^{(0)}$ are selected, and the initial values can be approximated by the graphical method. Substituting these initial values into equations (11)–(15), the iterative increments ($\Delta L_{A'A}^{(0)}$, $\Delta\theta_2^{(0)}$, $\Delta\theta_3^{(0)}$, and $\Delta\theta_4^{(0)}$) and the next iteration variables can be obtained as follows:

$$\varphi_j^{(1)} = \varphi_j^{(0)} + \Delta\varphi_j^{(0)}, \quad (j = 1, \ldots, 4), \tag{17}$$

where $\varphi_1, \varphi_2, \varphi_3$, and φ_4 represent $L_{A'A}$, θ_2, θ_3, and θ_4 and $\Delta\varphi_1^{(0)}$, $\Delta\varphi_2^{(0)}$, $\Delta\varphi_3^{(0)}$, and $\Delta\varphi_4^{(0)}$ represent $\Delta L_{A'A}^{(0)}$, $\Delta\theta_2^{(0)}$, $\Delta\theta_3^{(0)}$, and $\Delta\theta_4^{(0)}$, respectively.

Thus, the displacement functions of the first iteration $f_i^{(1)}$ ($i = 1, \ldots, 4$) can be calculated. Repeat iteratively until the r times, if

$$\left|f_i^{(r)}\right| \le \varepsilon_i, \quad i = 1, \ldots, 4, \tag{18}$$

the iterative procedure stops, where ε_i is the calculation accuracy set for each function f_i.

$L_{A'A}$, θ_2, θ_3, and θ_4 in the matrix can be solved by the subroutine of the Gaussian principal elimination method of solving the linear equations. Its iterative block diagram is shown in Figure 4.

2.3. Velocity Analysis

2.3.1. Velocity Analysis of the Source Phase. Differentiating equations (5) and (6) with respect to time yields

$$\begin{cases} -L_{OA'}\dot{\theta}_1\sin\theta_1 - \dot{L}_{A'A}\sin\theta_1 - L_{A'A}\dot{\theta}_1\cos\theta_1 + L_{AB}\dot{\theta}_2\sin\theta_2 - \dot{L}_{BD}\cos\theta_4 + L_{BD}\dot{\theta}_4\sin\theta_4 = 0, \\ L_{OA'}\dot{\theta}_1\cos\theta_1 + \dot{L}_{A'A}\cos\theta_1 - L_{A'A}\dot{\theta}_1\sin\theta_1 - L_{AB}\dot{\theta}_2\cos\theta_2 - \dot{L}_{BD}\sin\theta_4 - L_{BD}\dot{\theta}_4\cos\theta_4 = 0, \end{cases} \tag{19}$$

$$\begin{cases} -L_{OA'}\dot{\theta}_1\sin\theta_1 - \dot{L}_{A'A}\sin\theta_1 - L_{A'A}\dot{\theta}_1\cos\theta_1 - L_{AC}\dot{\theta}_2\sin\theta_2 - \dot{L}_{CE}\cos\theta_3 + L_{CE}\dot{\theta}_3\sin\theta_3 = 0, \\ L_{OA'}\dot{\theta}_1\cos\theta_1 + \dot{L}_{A'A}\cos\theta_1 - L_{A'A}\dot{\theta}_1\sin\theta_1 + L_{AC}\dot{\theta}_2\cos\theta_2 - \dot{L}_{CE}\sin\theta_3 - L_{CE}\dot{\theta}_3\cos\theta_3 = 0. \end{cases} \tag{20}$$

Equations (19) and (20) can be simplified as follows:

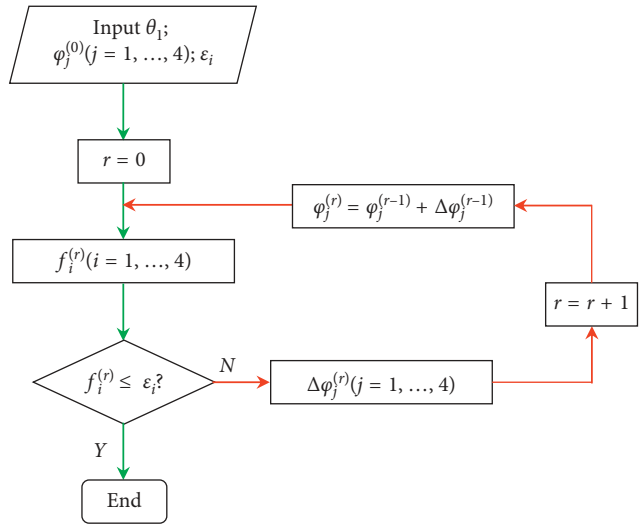

Figure 4: The block diagram of the Newton–Raphson method.

$$\begin{cases} -L_{OA'}\dot{\theta}_1 \sin(\theta_1 - \theta_4) - L_{A'A}\dot{\theta}_1 \cos(\theta_1 - \theta_4) + L_{AB}\dot{\theta}_2 \sin(\theta_2 - \theta_4) - \dot{L}_{A'A} \sin(\theta_1 - \theta_4) = \dot{L}_{BD}, \\ -L_{OA'}\dot{\theta}_1 \sin(\theta_1 - \theta_3) - L_{A'A}\dot{\theta}_1 \cos(\theta_1 - \theta_3) - L_{AC}\dot{\theta}_2 \sin(\theta_2 - \theta_3) - \dot{L}_{A'A} \sin(\theta_1 - \theta_3) = \dot{L}_{CE}. \end{cases} \tag{21}$$

Supposing $\boldsymbol{\omega}_1 = \begin{bmatrix} \dot{\theta}_1 & \dot{\theta}_2 & \dot{L}_{A'A} \end{bmatrix}^{\mathrm{T}}$ is the velocity vector of Cartesian coordinates and $\mathbf{v}_1 = \begin{bmatrix} \dot{L}_{BD} & \dot{L}_{CE} \end{bmatrix}^{\mathrm{T}}$ is the velocity vector of actuated joint coordinates, equation (21) can be written as the matrix form:

$$\mathbf{J}_{a1}\boldsymbol{\omega}_1 = \mathbf{J}_{b1}\mathbf{v}_1. \tag{22}$$

The velocity equation also can be obtained as follows:

$$\mathbf{v}_1 = \mathbf{J}_{b1}^{-1}\mathbf{J}_{a1}\boldsymbol{\omega}_1, \tag{23}$$

where

$$\begin{aligned} \mathbf{J}_{a1} &= \begin{bmatrix} -L_{OA'} \sin(\theta_1 - \theta_4) - L_{A'A} \cos(\theta_1 - \theta_4) & L_{AB} \sin(\theta_2 - \theta_4) & -\sin(\theta_1 - \theta_4) \\ -L_{OA'} \sin(\theta_1 - \theta_3) - L_{A'A} \cos(\theta_1 - \theta_3) & -L_{AC} \sin(\theta_2 - \theta_3) & -\sin(\theta_1 - \theta_3) \end{bmatrix}, \\ \mathbf{J}_{b1} &= \begin{bmatrix} 1 & 0 \\ 0 & 1 \end{bmatrix}. \end{aligned} \tag{24}$$

2.3.2. Velocity Analysis of the Adjustment Phase. As shown in Figure 3(b), the vector of Cartesian coordinates can be expressed as $\boldsymbol{\omega}_2 = \begin{bmatrix} \dot{\theta}_2 & \dot{L}_{A'A} \end{bmatrix}^{\mathrm{T}}$, and the vector of actuated joint coordinates can be expressed as $\mathbf{v}_2 = \begin{bmatrix} \dot{L}_{BD} & \dot{L}_{CE} \end{bmatrix}^{\mathrm{T}}$. Thus, equation (21) can be written as the matrix form:

$$\mathbf{J}_{a2}\boldsymbol{\omega}_2 = \mathbf{J}_{b2}\mathbf{v}_2. \tag{25}$$

The velocity equation in the adjustment phase can be expressed as

$$\mathbf{v}_2 = \mathbf{J}_{b2}^{-1}\mathbf{J}_{a2}\boldsymbol{\omega}_2, \tag{26}$$

where

$$\begin{aligned} \mathbf{J}_{a2} &= \begin{bmatrix} L_{AB} \sin(\theta_2 - \theta_4) & -\sin(\theta_1 - \theta_4) \\ -L_{AC} \sin(\theta_2 - \theta_3) & -\sin(\theta_1 - \theta_3) \end{bmatrix}, \\ \mathbf{J}_{b2} &= \begin{bmatrix} 1 & 0 \\ 0 & 1 \end{bmatrix}. \end{aligned} \tag{27}$$

2.3.3. Velocity Analysis of the Normal Working Phase. When the mechanism changes to the normal working phase, the two hydraulic cylinders are locked and the springs are in an equilibrium position, so $\dot{\theta}_3$, $\dot{\theta}_4$, $\dot{L}_{BD}$, and $\dot{L}_{CE}$ are all zero.

2.3.4. Velocity Analysis of the Special Phase. Supposing that the vector of Cartesian coordinates is expressed as $\boldsymbol{\omega}_4 =$

$\left[\dot{\theta}_2 \ \dot{\theta}_3 \ \dot{\theta}_4 \ \dot{L}_{A'A}\right]^{\mathrm{T}}$ and the vector of actuated joint coordinates is expressed as $\mathbf{v}_4 = [\dot{\theta}_1]^{\mathrm{T}}$. Differentiating equations (11)–(14) with respect to time yields

$$\mathbf{J}_{a4}\boldsymbol{\omega}_4 = \mathbf{J}_{b4}\mathbf{v}_4. \tag{28}$$

The velocity equations in the special phase can be obtained as

$$\boldsymbol{\omega}_4 = \mathbf{J}_{a4}^{-1}\mathbf{J}_{b4}\mathbf{v}_4, \tag{29}$$

where

$$\mathbf{J}_{a4} = \begin{bmatrix} L_{AB}\sin\theta_2 & 0 & L_{BD}\sin\theta_4 & \sin\theta_1 \\ -L_{AB}\cos\theta_2 & 0 & -L_{BD}\cos\theta_4 & -\cos\theta_1 \\ -L_{AC}\sin\theta_2 & L_{CE}\sin\theta_3 & 0 & \sin\theta_1 \\ L_{AC}\cos\theta_2 & -L_{CE}\cos\theta_3 & 0 & -\cos\theta_1 \end{bmatrix},$$
$$\mathbf{J}_{b4} = \begin{bmatrix} -L_{OA'}\sin\theta_1 + L_{A'A}\cos\theta_1 \\ L_{OA'}\cos\theta_1 + L_{A'A}\sin\theta_1 \\ -L_{OA'}\sin\theta_1 + L_{A'A}\cos\theta_1 \\ L_{OA'}\cos\theta_1 + L_{A'A}\sin\theta_1 \end{bmatrix}. \tag{30}$$

2.4. Acceleration Analysis

2.4.1. Acceleration Analysis of the Source Phase. Taking equations (7) and (8) into equation (23), its time derivative can be obtained:

$$\mathbf{a}_1 = \mathbf{E}\boldsymbol{\alpha}_1 + \mathbf{H}\begin{bmatrix} \dot{\theta}_1^2 \\ \dot{\theta}_2^2 \\ \dot{L}_{A'A}^2 \end{bmatrix} + \mathbf{G}\begin{bmatrix} \dot{\theta}_1\dot{\theta}_2 \\ \dot{\theta}_1\dot{L}_{A'A} \\ \dot{\theta}_2\dot{L}_{A'A} \end{bmatrix}, \tag{31}$$

where

$$\mathbf{E} = \begin{bmatrix} e_{11} & e_{12} & e_{13} \\ e_{21} & e_{22} & e_{23} \end{bmatrix},$$
$$\mathbf{H} = \begin{bmatrix} h_{11} & h_{12} & h_{13} \\ h_{21} & h_{22} & h_{23} \end{bmatrix}, \tag{32}$$
$$\mathbf{G} = \begin{bmatrix} g_{11} & g_{12} & g_{13} \\ g_{21} & g_{22} & g_{23} \end{bmatrix},$$

where $\mathbf{a}_1 = \left[\ddot{L}_{BD} \ \ddot{L}_{CE}\right]^{\mathrm{T}}$ is the acceleration vector of actuated joints and $\boldsymbol{\alpha}_1 = \left[\ddot{\theta}_1 \ \ddot{\theta}_2 \ \ddot{L}_{A'A}\right]^{\mathrm{T}}$ is the acceleration vector of Cartesian coordinates. e_{ij}, h_{ij}, and g_{ij} are the variables related to the posture of the mechanism ($i = 1, 2$; $j = 1, 2, 3$).

2.4.2. Acceleration Analysis of the Adjustment Phase. Taking equations (7) and (8) into equation (26), its time derivative can be obtained:

$$\mathbf{a}_2 = \mathbf{W}\boldsymbol{\alpha}_2 + \mathbf{P}\begin{bmatrix} \dot{\theta}_2^2 \\ \dot{\mathbf{L}}_{A'A}^2 \end{bmatrix} + q\dot{\theta}_2\dot{\mathbf{L}}_{A'A}, \tag{33}$$

where

$$\mathbf{W} = \begin{bmatrix} w_{11} & w_{12} \\ w_{21} & w_{22} \end{bmatrix},$$
$$\mathbf{P} = \begin{bmatrix} p_{11} & p_{12} \\ p_{21} & p_{22} \end{bmatrix}, \tag{34}$$

where $\mathbf{a}_2 = \left[\ddot{L}_{BD} \ \ddot{L}_{CE}\right]^{\mathrm{T}}$ is the acceleration matrix of actuated joints and $\boldsymbol{\alpha}_2 = \left[\ddot{\theta}_2 \ \ddot{L}_{A'A}\right]^{\mathrm{T}}$ is the acceleration vector of Cartesian coordinates; w_{ij}, p_{ij}, and q are the variables related to the pose of the mechanism ($i = 1, 2$; $j = 1, 2$).

2.4.3. Acceleration Analysis of the Normal Working Phase. When the mechanism changes to the normal working phase, the two hydraulic cylinders are locked and the springs are in an equilibrium position, so $\ddot{\theta}_3$, $\ddot{\theta}_4$, $\ddot{L}_{BD}$, and $\ddot{L}_{CE}$ are all zero.

2.4.4. Acceleration Analysis of the Special Phase. Taking equations (7) and (8) into equation (29), its time derivative can be obtained:

$$\boldsymbol{\alpha}_4 = \mathbf{Z}\mathbf{a}_4 + \mathbf{X}\begin{bmatrix} \dot{\theta}_1^2 \\ \dot{\theta}_1\dot{\theta}_2 \\ \dot{\theta}_1\dot{L}_{A'A} \end{bmatrix}, \tag{35}$$

where

$$\mathbf{Z} = \left[z_{11} \ z_{12} \ z_{13} \ z_{14}\right]^{\mathrm{T}},$$
$$\mathbf{X} = \begin{bmatrix} x_{11} & x_{12} & x_{13} \\ x_{21} & x_{22} & x_{23} \\ x_{31} & x_{32} & x_{33} \\ x_{41} & x_{42} & x_{43} \end{bmatrix}, \tag{36}$$

where $\mathbf{a}_4 = [\ddot{\theta}_1]$ is the acceleration vector of actuated joint, $\boldsymbol{\alpha}_4 = \left[\ddot{\theta}_2 \ \ddot{\theta}_3 \ \ddot{\theta}_4 \ \ddot{L}_{A'A}\right]^{\mathrm{T}}$ is the acceleration vector of Cartesian coordinates, and z_{ij} and x_{ij} are the variables related to the posture of the mechanism ($i = 1, 2, 3, 4$; $j = 1, 2, 3, 4$).

3. Dynamic Analysis

The velocity and acceleration of each component obtained through the above kinematic analysis can be used to establish the inverse dynamic models of the CMRP. The results of dynamic analysis will be used for simulations, actuator selection, mechanical vibration analysis, and dynamic optimization. More importantly, the precision of the CMRP definitely relies on the dynamic properties.

3.1. Dynamic Analysis of the Source Phase. Kinematic analysis must be performed together with dynamic analysis for the CMRP, as mentioned in Section 2.2.1. In order to solve

the force of each component conveniently, the Newton–Euler method is used to establish its dynamic model. However, for the metamorphic mechanism with force constraint, if the Newton–Euler method is directly used, the listed equations will be highly complex nonlinear differential algebraic equations and the number of equations is excessive, which will make it difficult to solve the equations.

From the energy view point, the dynamic equations obtained by the Lagrange method are relatively simple, and the number of equations is only related to the DOF of the mechanism. In addition, there is no external force input at the prismatic joint P_3 for the mechanism with force constraint proposed in this paper.

Therefore, a solving method combining Lagrange equation with the Newton–Euler equation is presented. Firstly, according to no external force input at the prismatic joint P_3, the kinematics equation and dynamics equation are solved simultaneous by the Lagrange method. Then, the displacement, velocity, and acceleration of slider are obtained, which are brought into Newton–Euler equations. Finally, the equations are transformed into algebraic equations, which effectively improve the efficiency of solving the nonlinear differential algebraic equations and reduce the difficulty.

When modeling the system dynamics based on the Lagrange equation, the generalized coordinates of the system are selected first, and then the expressions of kinetic energy, potential energy, and generalized force of the system are obtained. Substituting into the Lagrange equation, the system dynamic equation can be derived as follows:

$$\frac{d}{dt}\left(\frac{\partial T}{\partial \dot{q}_i}\right) - \frac{\partial T}{\partial q_i} + \frac{\partial U}{\partial q_i} = Q_i, \quad i = 1, 2, \ldots, n, \tag{37}$$

where n is the DOF of the system, q_i denotes the generalized coordinates, U is the total potential energy of the system, T is the total kinetic energy of the system, and Q_i represents the generalized force corresponding to q_i.

3.1.1. Total Potential Energy of the Source Phase. For convenience, set m_1, m_2, m_3, m_4, m_5, m_6, and m_7 as the masses of the rotary plough frame, the slider, the compatibility rod, the left cylinder rod, the corresponding left cylinder, the right cylinder rod, and the corresponding right cylinder, respectively; set s_1, s_2, s_3, s_4, s_5, s_6, and s_7 as the centroids of the rotary plough frame, the slider, the compatibility rod, the left cylinder rod, the corresponding left cylinder, the right cylinder rod, and corresponding right cylinder, respectively. The positions of s_2 and s_3 coincide with the position of joint A; for convenience, they are not marked in the figures. The centroid coordinates of each component can be written as follows:

$$\begin{cases} x_1 = -r_1 \cos(\beta - \theta_1), \\ y_1 = r_1 \sin(\beta - \theta_1), \end{cases} \tag{38}$$

$$\begin{cases} x_2 = L_{OA'} \cos\theta_1 - L_{A'A} \sin\theta_1, \\ y_2 = L_{OA'} \sin\theta_1 + L_{A'A} \cos\theta_1, \end{cases} \tag{39}$$

$$\begin{cases} x_3 = L_{OA'} \cos\theta_1 - L_{A'A} \sin\theta_1, \\ y_3 = L_{OA'} \sin\theta_1 + L_{A'A} \cos\theta_1, \end{cases} \tag{40}$$

$$\begin{cases} x_4 = L_{OA'} \cos\theta_1 - L_{A'A} \sin\theta_1 + L_{AC} \cos\theta_2 - r_4 \cos\theta_3, \\ y_4 = L_{OA'} \sin\theta_1 + L_{A'A} \cos\theta_1 + L_{AC} \sin\theta_2 - r_4 \sin\theta_3, \end{cases} \tag{41}$$

$$\begin{cases} x_5 = -L_{GE} + r_5 \cos\theta_3, \\ y_5 = L_{OG} + r_5 \sin\theta_3, \end{cases} \tag{42}$$

$$\begin{cases} x_6 = L_{OA'} \cos\theta_1 - L_{A'A} \sin\theta_1 - L_{AB} \cos\theta_2 - r_6 \cos\theta_4, \\ y_6 = L_{OA'} \sin\theta_1 + L_{A'A} \cos\theta_1 - L_{AB} \sin\theta_2 - r_6 \sin\theta_4, \end{cases} \tag{43}$$

$$\begin{cases} x_7 = L_{GD} + r_7 \cos\theta_4, \\ y_7 = L_{OG} + r_7 \sin\theta_4. \end{cases} \tag{44}$$

The total potential energy of the CMRP can be obtained from equations (38)–(44) as follows:

$$U_{\text{all}} = \sum_{i=1}^{7} m_i g y_i + U_8, \quad i = 1, \ldots, 7. \tag{45}$$

in which U_8 is expressed as

$$U_8 = \left(\frac{1}{2} k L_{A'A}^2\right) \times 2, \tag{46}$$

where U_8 is the elastic potential energy, k is the elastic coefficient, and g is the gravitational acceleration along the negative direction of the y-axis.

3.1.2. Total Kinematic Energy of the Source Phase. All the components of the CMRP are moved in a plane, and the kinetic energy of each component can be expressed by the general formula as follows:

$$T = \frac{1}{2}\left[m\left(\dot{x}^2 + \dot{y}^2\right) + J\omega^2\right]. \tag{47}$$

According to equation (47), the kinetic energy of each component in the system can be obtained as

$$T_1 = \frac{1}{2} J_{1O} \dot{\theta}_1^2, \tag{48}$$

$$T_2 = \frac{1}{2} m_2 \left(\dot{x}_2^2 + \dot{y}_2^2\right) + \frac{1}{2} J_2 \dot{\theta}_1^2, \tag{49}$$

$$T_3 = \frac{1}{2} m_3 \left(\dot{x}_3^2 + \dot{y}_3^2\right) + \frac{1}{2} J_3 \dot{\theta}_2^2, \tag{50}$$

$$T_4 = \frac{1}{2} m_4 \left(\dot{x}_4^2 + \dot{y}_4^2\right) + \frac{1}{2} J_4 \dot{\theta}_3^2, \tag{51}$$

$$T_5 = \frac{1}{2} J_{5E} \dot{\theta}_3^2, \tag{52}$$

$$T_6 = \frac{1}{2}m_6\left(\dot{x}_6^2 + \dot{y}_6^2\right) + \frac{1}{2}J_6\dot{\theta}_4^2, \tag{53}$$

$$T_7 = \frac{1}{2}J_{7D}\dot{\theta}_4^2, \tag{54}$$

in which J_{1O} is the moment of inertia of the rotary plough frame around the point O; J_{5E} is the moment of inertia of the cylinder of the left hydraulic cylinder around the point E; J_{7D} is the moment of inertia of the cylinder of the right hydraulic cylinder around the point D; and J_2, J_3, J_4, and J_6 denote the moment of inertia around centroid of the slider, the compatibility rod, the cylinder rod of left hydraulic cylinder, and the cylinder rod of right hydraulic cylinder, respectively.

The total kinetic energy of the system can be obtained from equations (48)–(54) as follows:

$$T_{\text{all}} = \sum_{i=1}^{7} T_i. \tag{55}$$

3.1.3. Establishing a Dynamic Model of the Source Phase Using the Lagrange Equation. In the source phase, the CMRP is a 3-DOF mechanical system and $L_{A'A}$, θ_1, and θ_2 are selected as generalized coordinates. As shown in Figure 2, the friction and clearance between the motion pairs and deformation of the components are ignored. Taking equations (38)–(55) into equation (37), the dynamic equations of the system can be written as follows:

$$0 = \frac{d}{dt}\left(\frac{\partial L}{\partial \dot{L}_{A'A}}\right) - \frac{\partial L}{\partial L_{A'A}}, \tag{56}$$

$$M_1 = \frac{d}{dt}\left(\frac{\partial L}{\partial \dot{\theta}_1}\right) - \frac{\partial L}{\partial \theta_1}, \tag{57}$$

$$M_2 = \frac{d}{dt}\left(\frac{\partial L}{\partial \dot{\theta}_2}\right) - \frac{\partial L}{\partial \theta_2}. \tag{58}$$

Dynamic analysis must be performed in conjunction with the kinematic analysis due to the CMRP being an underactuated mechanism during the source phase. On the basis, considered the theory that velocity and acceleration are the same in an extremely brief period, simultaneous equations (7)–(10) and (56) can be used to obtain the displacement, velocity, and acceleration of the slider. Then, the generalized moments M_1 and M_2 can be solved according to equations (57) and (58), respectively.

According to the virtual work principle, the relationship between the driving forces F_1 and F_2 of the two hydraulic cylinders and the generalized moments M_1 and M_2 can be derived as follows:

$$F_1\delta L_{CE} + F_2\delta L_{BD} + F_3\delta L_{A'A} = M_1\delta\theta_1 + M_2\delta\theta_2. \tag{59}$$

Substituting equations (9) and (10) into equation (59) leads to

$$\begin{aligned}&(AF_1 + CF_2)\delta\theta_1 + (BF_1 + DF_2)\delta\theta_2 + (EF_1 + FF_2 - F_3)\delta L_{A'A}\\ &\quad = M_1\delta\theta_1 + M_2\delta\theta_2,\end{aligned} \tag{60}$$

in which

$$\begin{aligned}
a &= L_{OA'}\cos\theta_1 - L_{A'A}\sin\theta_1 + L_{AC}\cos\theta_2 + L_{GE},\\
b &= L_{OA'}\sin\theta_1 + L_{A'A}\cos\theta_1 + L_{AC}\sin\theta_2 - L_{OG},\\
c &= L_{OA'}\cos\theta_1 - L_{A'A}\sin\theta_1 - L_{AB}\cos\theta_2 - L_{GD},\\
d &= L_{OA'}\sin\theta_1 + L_{A'A}\cos\theta_1 - L_{AB}\sin\theta_2 - L_{OG},\\
A &= \left(a^2 + b^2\right)^{-(1/2)}\Big[a\left(-L_{OA'}\sin\theta_1 - L_{A'A}\cos\theta_1\right)\\
&\quad + b\left(L_{OA'}\cos\theta_1 - L_{A'A}\sin\theta_1\right)\Big],\\
B &= \left(a^2 + b^2\right)^{-(1/2)}\left(-aL_{AC}\sin\theta_2 + bL_{AC}\cos\theta_2\right),\\
C &= \left(c^2 + d^2\right)^{-(1/2)}\Big[c\left(-L_{OA'}\sin\theta_1 - L_{A'A}\cos\theta_1\right)\\
&\quad + d\left(L_{OA'}\cos\theta_1 - L_{A'A}\sin\theta_1\right)\Big],\\
D &= \left(c^2 + d^2\right)^{-(1/2)}\left(cL_{AB}\sin\theta_2 - dL_{AB}\cos\theta_2\right).
\end{aligned} \tag{61}$$

According to equation (60), the driving forces F_1 and F_2 of the two hydraulic cylinders can be expressed as

$$\begin{aligned}
F_1 &= \frac{DM_1 - CM_2}{AD - BC},\\
F_2 &= \frac{BM_1 - AM_2}{BC - AD}.
\end{aligned} \tag{62}$$

3.1.4. Establishing a Dynamic Model of the Source Phase Using the Newton–Euler Method. The velocity and acceleration of each component obtained through the above analysis can be used to establish the inverse dynamic model of the CMRP. The advantage of the Newton–Euler method is that, unlike other methods, this method not only can solve the driving forces but also can obtain the internal forces and moments applied to the passive joints. It is essential for engineering design applications such as selection of bearings and materials and design of the links.

The force analysis diagram of the rotary plough frame is shown in Figure 5. In the analysis, it is assumed that the centroid of the rotary plough frame is located at the geometric center, and the self-gravity of this linkage is G_1.

According to the D'Alembert principle, the dynamic equations of the rotary plough frame can be derived as follows:

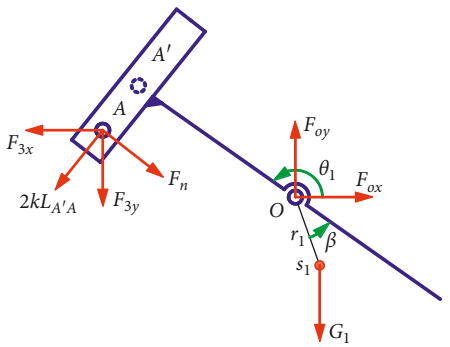

Figure 5: The force analysis diagram of the rotary plough frame during the source phase.

$$F_{ox} - F_n \cos\theta_1 - 2kL_{A'A} \sin\theta_1 - F_{3x} - m_1\ddot{x}_1 = 0, \quad (63)$$

$$F_{oy} - F_n \sin\theta_1 + 2kL_{A'A} \cos\theta_1 - F_{3y} - G_1 - m_1\ddot{y}_1 = 0, \quad (64)$$

$$\begin{aligned} &F_n L_{A'A} + F_{3x}\left(L_{OA'} \sin\theta_1 + L_{A'A} \cos\theta_1\right) \\ &\quad + F_{3y}\left(-L_{OA'} \cos\theta_1 + L_{A'A} \sin\theta_1\right) + 2kL_{A'A}L_{OA'} \\ &\quad + G_1 r_1 \cos\left(\beta - \theta_1\right) - J_{1O}\ddot{\theta}_1 = 0, \end{aligned} \quad (65)$$

where F_{ox} and F_{oy} are the constraint forces of the joint O in the directions of the x and y, respectively, and F_n is the constraint force of the prismatic joint P_3.

The dynamic equations of the slider according to the D'Alembert principle, as shown in Figure 6, can be written as follows:

$$-F_{ax} + 2kL_{A'A} \sin\theta_1 - F_n \cos\theta_1 + F_{3x} - m_2\ddot{x}_2 = 0, \quad (66)$$

$$-F_{ay} + 2kL_{A'A} \cos\theta_1 + F_n \sin\theta_1 + F_{3y} - G_2 - m_2\ddot{y}_2 = 0, \quad (67)$$

where F_{ax} and F_{ay} are the constraint forces of the joint A in the directions of the x and y, respectively.

The dynamic equations of the compatibility rod according to the D'Alembert principle, as shown in Figure 7, can be written as follows:

$$F_{ax} + F_{bx} + F_{cx} - m_3\ddot{x}_3 = 0, \quad (68)$$

$$F_{ay} + F_{by} + F_{cy} - G_3 - m_3\ddot{y}_3 = 0, \quad (69)$$

$$\begin{aligned} &F_{bx}L_{AB} \sin\theta_2 - F_{by}L_{AB} \cos\theta_2 - F_{cx}L_{AC} \sin\theta_2 \\ &\quad + F_{cy}L_{AC} \cos\theta_2 - J_3\ddot{\theta}_2 = 0, \end{aligned} \quad (70)$$

where F_{bx} and F_{by} are the constraint forces of the joint B in the directions of the x and y, respectively, and F_{cx} and F_{cy} are the constraint forces of the joint C in the directions of the x and y, respectively.

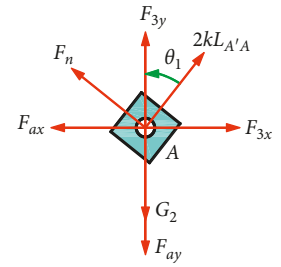

Figure 6: The force analysis diagram of the slider during the source phase.

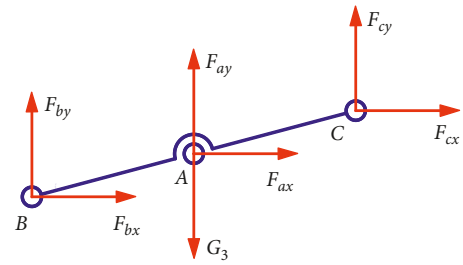

Figure 7: The force analysis diagram of the compatibility rod during the source phase.

The dynamic equations of the left hydraulic cylinder according to the D'Alembert principle, as shown in Figure 8, satisfies

$$-F_{cx} - F_{ex} - \left(m_4 + m_5\right)\ddot{x}_{45} = 0, \quad (71)$$

$$-F_{cy} - F_{ey} - G_{p1} - \left(m_4 + m_5\right)\ddot{y}_{45} = 0, \quad (72)$$

$$\begin{aligned} &F_{cx}\left(L_{CE} - L_{1c}\right)\sin\theta_3 - F_{cy}\left(L_{CE} - L_{1c}\right)\cos\theta_3 - F_{ex}L_{1c} \sin\theta_3 \\ &\quad + F_{ey}L_{1c} \cos\theta_3 - \left(J_4 + J_5\right)\ddot{\theta}_3 = 0, \end{aligned} \quad (73)$$

where F_{ex} and F_{ey} are the constraint forces of the joint E in the directions of the x and y, respectively, and in which

$$L_{1c} = \frac{m_5 r_5 + m_4\left(L_{CE} - r_4\right)}{m_4 + m_5},$$

$$\begin{cases} x_{45} = -L_{GE} + L_{1c} \cos\theta_3, \\ y_{45} = L_{OG} + L_{1c} \sin\theta_3, \end{cases} \quad (74)$$

$$G_{P1} = G_4 + G_5.$$

The dynamic equations of the right hydraulic cylinder according to the D'Alembert principle, as shown in Figure 9, satisfies

$$-F_{bx} - F_{dx} - \left(m_6 + m_6\right)\ddot{x}_{67} = 0, \quad (75)$$

$$-F_{by} - F_{dy} - G_{p2} - \left(m_6 + m_7\right)\ddot{y}_{67} = 0, \quad (76)$$

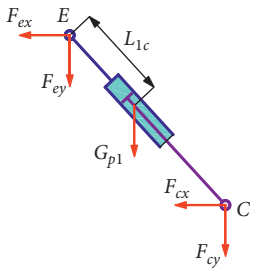

Figure 8: The force analysis diagram of the left hydraulic cylinder during the source phase.

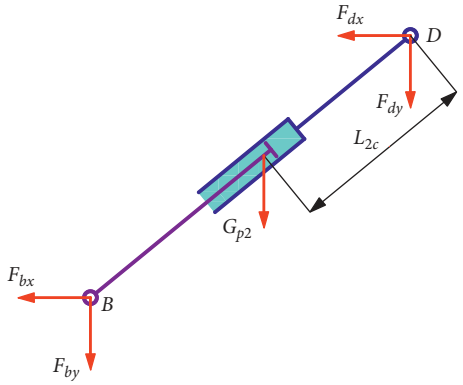

Figure 9: The force analysis diagram of the right hydraulic cylinder during the source phase.

$$F_{bx}(L_{BD} - L_{2c})\sin\theta_4 - F_{by}(L_{BD} - L_{2c})\cos\theta_4 - F_{dx}L_{2c}\sin\theta_4 + F_{dy}L_{2c}\cos\theta_4 - (J_6 + J_7)\ddot{\theta}_4 = 0, \tag{77}$$

where F_{dx} and F_{dy} are the constraint forces of the joint D in the directions of the x and y, respectively, and in which

$$L_{2c} = \frac{m_7 r_7 + m_7(L_{BD} - r_6)}{m_6 + m_7},$$

$$\begin{cases} x_{67} = L_{GD} + L_{2c}\cos\theta_4, \\ y_{67} = L_{OG} + L_{2c}\sin\theta_4, \end{cases} \tag{78}$$

$$G_{P2} = G_6 + G_7.$$

Then, the driving forces of the two hydraulic cylinders can be expressed as

$$F_{1x} = F_{cx} + m_4\ddot{x}_4, \tag{79}$$

$$F_{1y} = F_{cy} + G_4 + m_4\ddot{y}_4, \tag{80}$$

$$F_{2x} = F_{bx} + m_6\ddot{x}_6, \tag{81}$$

$$F_{2y} = F_{by} + G_6 + m_6\ddot{y}_6. \tag{82}$$

3.2. Dynamic Analysis of the Adjustment Phase. When the mechanism moves to the phase in Figure 3(b) where the joint O is locked, the mechanism is a 2-DOF mechanical system with two effective actuators at the two hydraulic cylinders. The required driving forces based on the Newton–Euler method can be directly obtained according to the motion laws of the slider and the compatibility rod.

The dynamic equations of the slider according to the D'Alembert principle, as shown in Figure 10, satisfies

$$\begin{aligned} -F_{ax} - m_2\ddot{x}_2 &= 0, \\ -F_{ay} + 2kL_{A'A} - G_2 - m_2\ddot{y}_2 &= 0. \end{aligned} \tag{83}$$

The force analysis diagrams of the compatibility rod and the two hydraulic cylinders are the same as Figures 7–9, respectively. Similarly, the dynamic equations of the compatibility rod and the two hydraulic cylinders can be expressed as equations (68)–(77), respectively.

Similarly, the driving forces of the two hydraulic cylinders can be expressed as the same as equations (79)–(82).

3.3. Dynamic Analysis of the Normal Working Phase. The driving forces of the two hydraulic cylinders and the internal forces applied to the passive joints, in the normal working phase, are the same as the end of the adjustment phase.

3.4. Dynamic Analysis of the Special Phase. The dynamic equations of the rotary plough frame according to the D'Alembert principle, as shown in Figure 11, satisfies

$$\begin{aligned} &F_{ox} - F_n\cos\theta_1 + 2kL_{A'A}\sin\theta_1 - m_1\ddot{x}_1 = 0, \\ &F_{oy} - F_n\sin\theta_1 - 2kL_{A'A}\cos\theta_1 + F - G_1 - m_1\ddot{y}_1 = 0, \\ &-F_nL_{A'A} - 2kL_{A'A}L_{OA'} + G_1r_1\cos(\beta - \theta_1) + Fl\cos\theta_1 - J_{1O}\ddot{\theta}_1 = 0, \end{aligned} \tag{84}$$

where F is the external force and l denotes the distance from the action point of the external force to joint O.

The dynamic equations of the slider according to the D'Alembert principle, as shown in Figure 12, satisfies

$$\begin{aligned} F_{ax} - 2kL_{A'A}\sin\theta_1 + F_n\cos\theta_1 - m_2\ddot{x}_2 &= 0, \\ F_{ay} + 2kL_{A'A}\cos\theta_1 + F_n\sin\theta_1 - G_2 - m_2\ddot{y}_2 &= 0. \end{aligned} \tag{85}$$

The dynamic analysis diagrams of the compatibility rod and the two hydraulic cylinders are the same as Figures 7–9, respectively. The dynamic equations of the compatibility rod and the two hydraulic cylinders can be expressed as equations (68)–(77), respectively.

4. Numerical Simulation and Performance Analysis

4.1. Determination of the Initial Position of the Springs. Determining the initial compression length of the spring with the elastic coefficient is one of the most basic things due

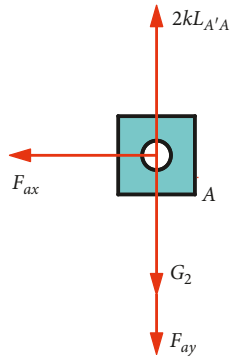

Figure 10: The force analysis diagram of the slider during the adjustment phase.

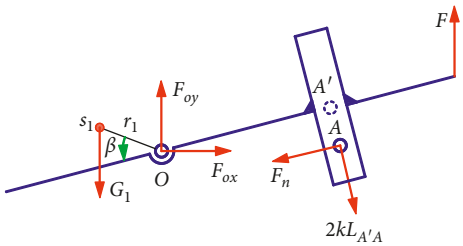

Figure 11: The dynamic analysis diagram of the rotary plough frame during the special phase.

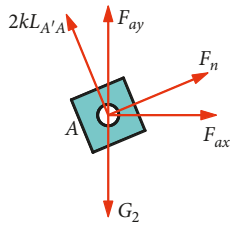

Figure 12: The dynamic analysis diagram of the slider during the special phase.

Table 1: Parameters of the CMRP.

Symbol	Values (unit)
$L_{OA'}$, L_{AC}, L_{AB}	0.3, 0.12, 0.12 (m)
r_1, r_3, r_4	0.088, 0, 0.267 (m)
m_1, m_2, m_3	84.633, 2.288, 5.6327 (kg)
J_{1O}, J_2, J_3	6.22, 0.002, 0.039 (kg·m^2)
β	1.311 (rad)
L_{GE}, L_{GD}, L_{OG}	0.4, 0.4, 0.75 (m)
r_5, r_6, r_7	0.27, 0.267, 0.27 (m)
m_4, m_5, m_6, m_7	4.78, 13.76, 4.78, 13.76 (kg)
J_4, J_{5E}, J_6, J_{7D}	0.15, 1.35, 0.15, 1.35 (kg·m^2)
g	9.8 (m/s^2)

to the dynamic equations of the CMRP being solved numerically. Assume that the elastic coefficient k is 0.08 N/m. When the initial compression lengths of the two springs are 0, combining Table 1, $L_{A'A}$ can be obtained numerically by solving equations (9), (10), and (56), as shown in Figure 13(a). As can be seen from Figure 13(a), the slider is in the vibrating state during the reversal process, which is determined by the initial compression length of the spring.

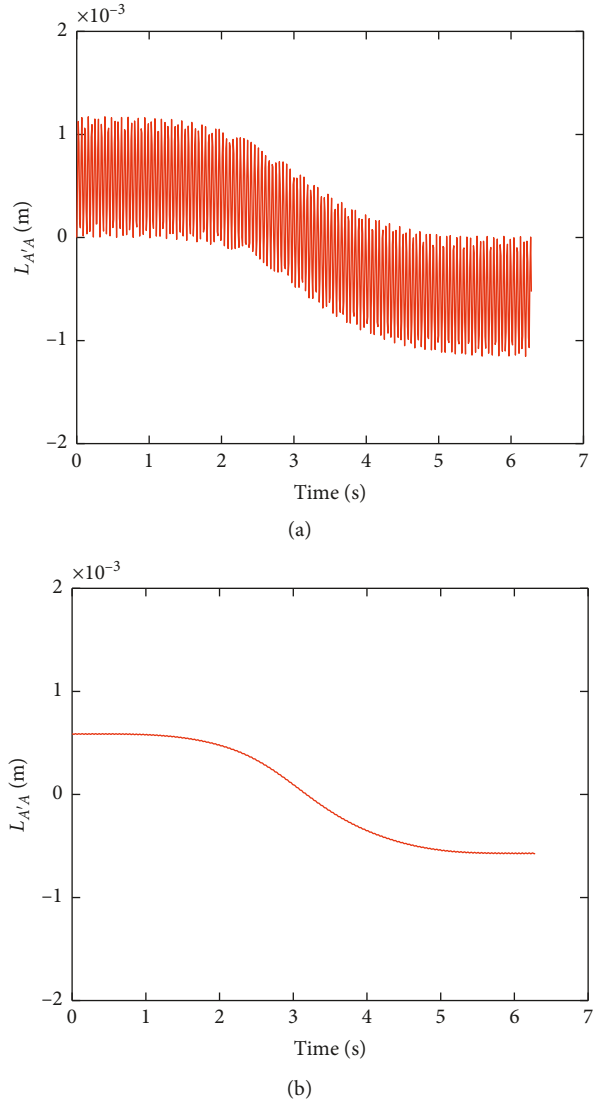

Figure 13: Displacement of slider in the source phase. Initial spring deformation: (a) 0 m; (b) 0.00059 m.

Therefore, the static balance analysis of the CMRP can be performed by changing the acceleration of each component in equations (63)–(82) to 0, and $L_{A'A}$ can be solved (the initial compression length of the spring is 0.00059 m), as shown in Figure 13(b). As can be seen from Figure 13(b), with this initial spring constant, the non-hesitating motion of the slider during the reversal process can be achieved.

4.2. Kinematic Numerical Simulations. Table 1 presents all of the related parameters: the structure parameters $L_{OA'}$, L_{AC}, L_{AB}, L_{GE}, L_{GD}, L_{OG}, r_1, r_3, r_4, r_5, r_6, r_7, α_1, and g; the

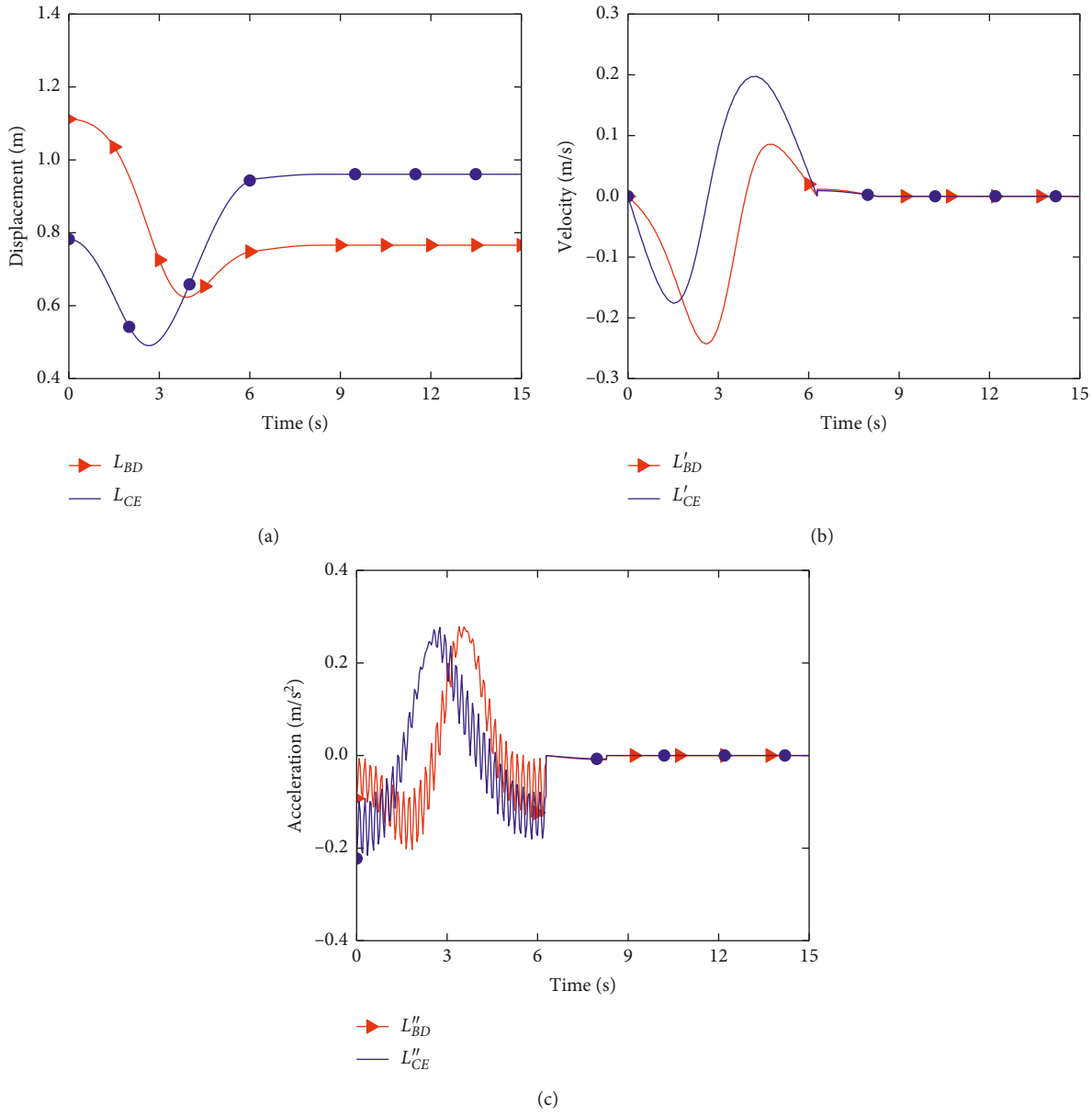

Figure 14: Kinematic simulation from the Matlab software: (a) displacements curves; (b) velocity curves; (c) acceleration curves.

component masses m_1, m_2, m_3, m_4, m_5, m_6, and m_7; and the moments of inertia J_{1O}, J_2, J_3, J_4, J_{5E}, J_6, and J_{7D}.

From the above analysis, the kinematic numerical simulations in the source phase can be obtained by equations (7)–(10) and (56), in the adjustment phase by equations (7)–(10), and the kinematic numerical simulations in the normal working phase stay the same as the state at the end of the adjustment phase, and in the special phase by equations (15) and (17). And Figure 14 shows the curves obtained from Matlab software, among which (a)–(c) reflect the displacements, velocities, and accelerations of the two hydraulic cylinders.

In order to verify the numerical example, the results obtained by means of the kinematic models are compared with the simulation results by creating the 3D model in SolidWorks software. Under SolidWorks environment, the structure parameters and initial kinematic parameters are the same as the previous analytical model. The simulation results generated in SolidWorks software are shown in Figure 15, among which (a)–(c) reflect the displacements, velocities, and accelerations of the two hydraulic cylinders, respectively.

By comparing the curves shown in Figures 14 and 15, we can see that the variation tendencies of the results obtained by the two programs are identical. This is sufficient to guarantee the correct of the theoretical kinematic models.

4.3. Dynamic Numerical Simulations and Contrast Analysis. To verify the above dynamic models of the CMRP, the same operations as the above kinematic analysis are done. And

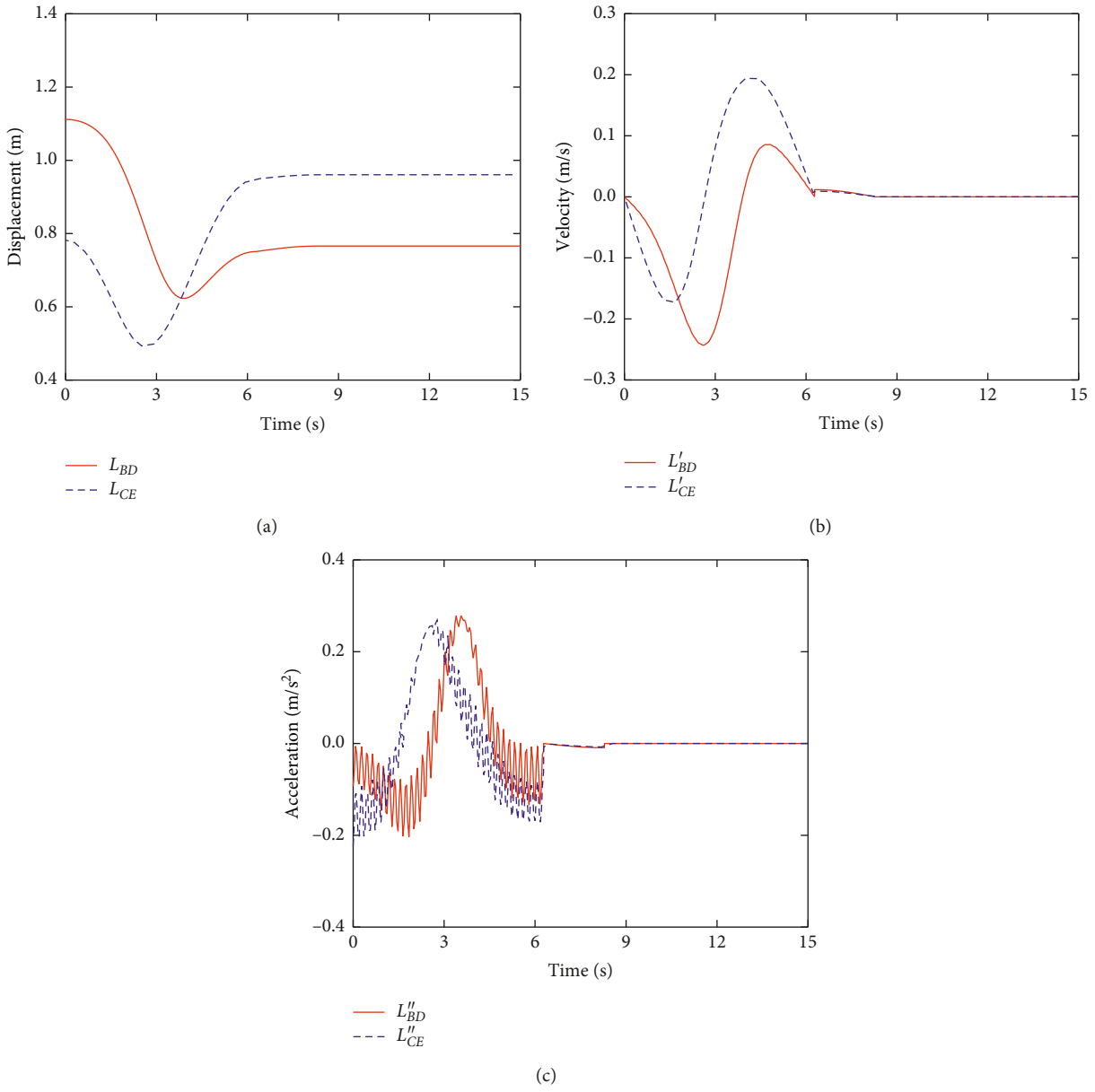

FIGURE 15: Kinematic simulation from the SolidWorks software: (a) displacement curves; (b) velocity curves; (c) acceleration curves.

then the results from the two different programs are shown in Figures 16(a) and 16(b) reflecting the actuation forces of the two hydraulic cylinders from the Matlab and SolidWorks software, respectively. Furthermore, the relative error analysis is given in Figure 16(c) in order to guarantee the accurate result.

Figure 16(c) shows that the maximal relative error of the actuation forces is less than 0.045. It is known that the dynamic simulation results are in excellent agreement with the analytic results derived from the analytic method. And the actuation forces can judge the loading characteristics of the actuators. Except that, the internal forces acting on revolute joints can help us to judge the joints stiffness. Here, the revolute joints related to the slider and the coordinated linkage are picked out as examples, and the joint forces are obtained; the internal forces acting on the revolute joints are shown in Figure 17.

Figure 17(a) shows the joint force F_a of the revolute joint located at point A; Figure 17(b) shows the joint force F_b of the revolute joint located at point B; and Figure 17(c) shows the joint force F_c of the revolute joint located at point C. From the results shown in Figure 17, we know that all of these three joint forces change comparatively smooth and steadily in the first three configurations. When the CMRP is in the special phase, all of these three joint forces change a lot under the effect of uncertain external force.

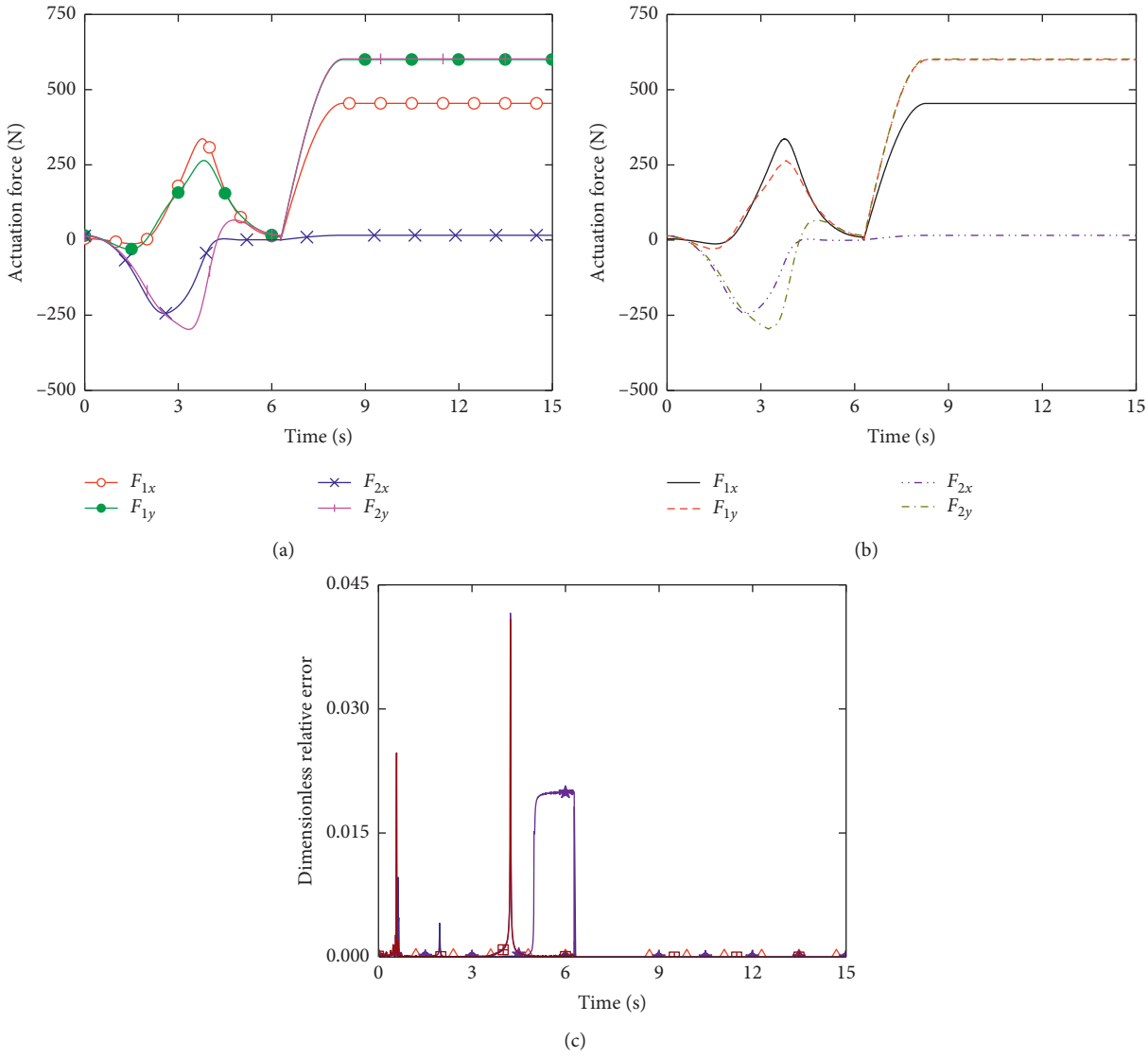

Figure 16: Dynamic simulations of the CMRP: (a) Matlab simulation; (b) SolidWorks simulation; (c) relative error.

4.4. Experimental Verification. An experimental trajectory has been designed to conduct the experiment and measured the displacements of the two hydraulic cylinders. In this paper, the electrohydraulic servo control system can be used to control the position of the two hydraulic cylinders, and the block diagram of the control system is shown in Figure 18. When the displacement command signals L_i of the two hydraulic cylinders are input into the given potentiometer, the corresponding voltage signals U_{1i} are generated and transmitted to the amplifier, and the amplifier converts voltage signal U_{1i} to current signal I_i and applies it to the position feedback electrohydraulic servo valve. The flows Q_i are obtained by the proportional relationship between the output signal current of the electrohydraulic servo valve and the input signal current, which makes the hydraulic cylinder move. Then, the displacements L_{i0} of the two hydraulic cylinders measured by the measuring element are fed back to the input end of the system by the voltage signals U_{2i} generated by the feedback potentiometer. Finally, compared with the input signals U_{1i}, the deviation signals are amplified and corrected and applied to the electrohydraulic servo valve to drive the hydraulic cylinder to move in the direction of eliminating the deviation until the deviation approaches zero.

On the basis, the principle prototype of the CMRP is built. Due to the limited experimental space, only the experiments of the source phase and the adjustment phase are carried out. As shown in Figure 19, the automatic operation mode of the CMRP prototype is started after the parameters related to the test are input into the control system through the operation panel. When the rotary plough frame is turned over to 180°, the CMRP prototype is stopped. Then, the displacement data of the hydraulic cylinder collected by the displacement sensor are derived. Finally, the comparisons between theoretical displacement and measured displacement are shown in Figure 20.

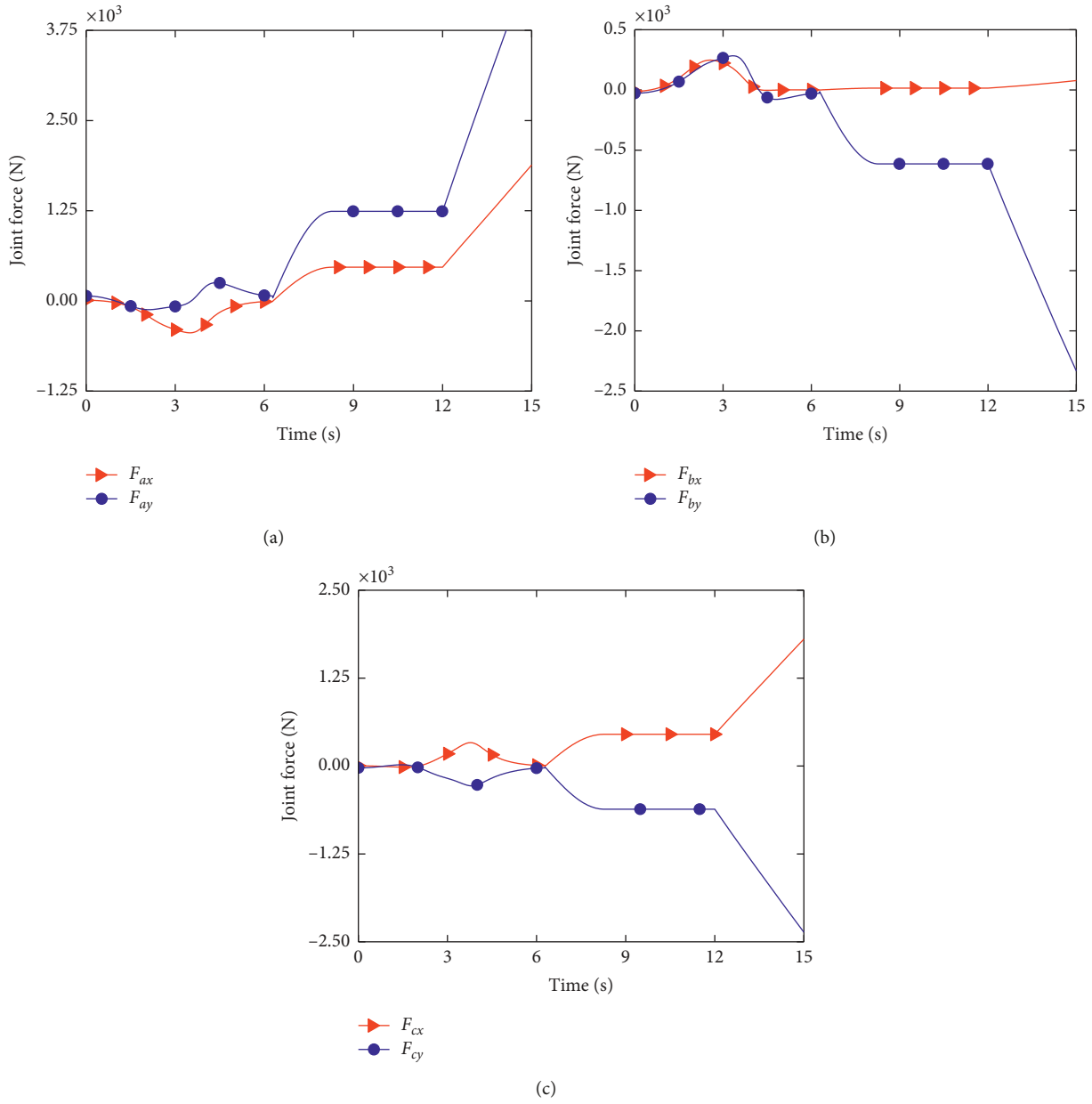

FIGURE 17: Joint force of the CMRP: (a) forces at joint A; (b) forces at joint B; (c) forces at joint C.

From Figure 20, we can see the trend of the two curves is generally the same. On the contrary, this also verifies the correctness of the theoretical model. But there is a sight difference between the two curves through the comparisons. Through the analysis, we can know the main reasons that caused the difference between the two curves:

(1) *Construction Error*. When the prototype is built, the size and shape of actual parts are not exactly the same as the simulation model. In the dynamic model, the parameters of the CMRP are identical but different in the actual part. The assembly clearances between the parts are not considered in the dynamic model. These errors can lead to many differences between theory and reality.

(2) *Measurement Error*. When we measure the displacements of the two hydraulic cylinders, the measuring instrument has certain accuracy. In addition, the structure of the instrument cannot be guaranteed to satisfy various geometric relations during the process and assemblies. Such an instrument will inevitably bring errors to the measurement.

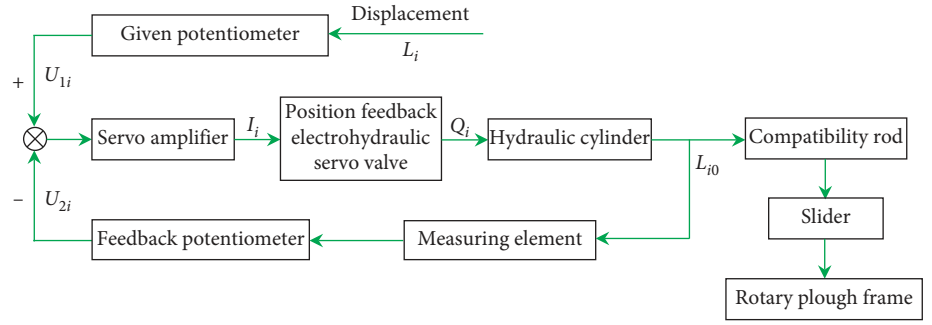

Figure 18: Block diagram of the control system.

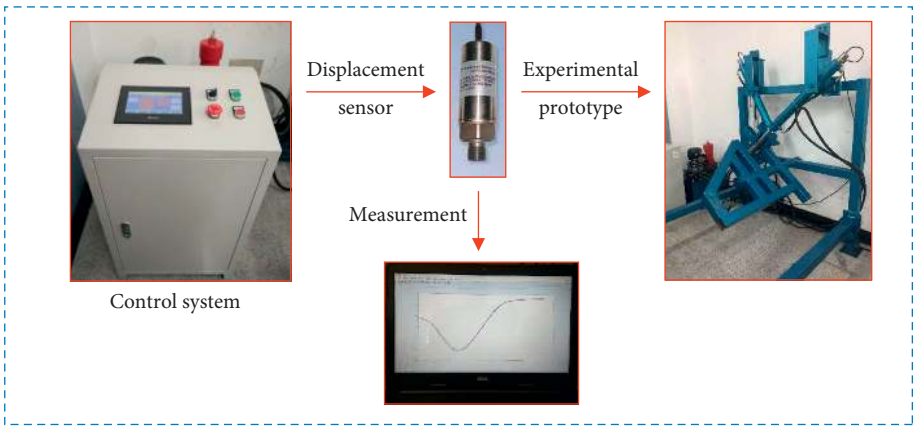

Figure 19: Experimental process.

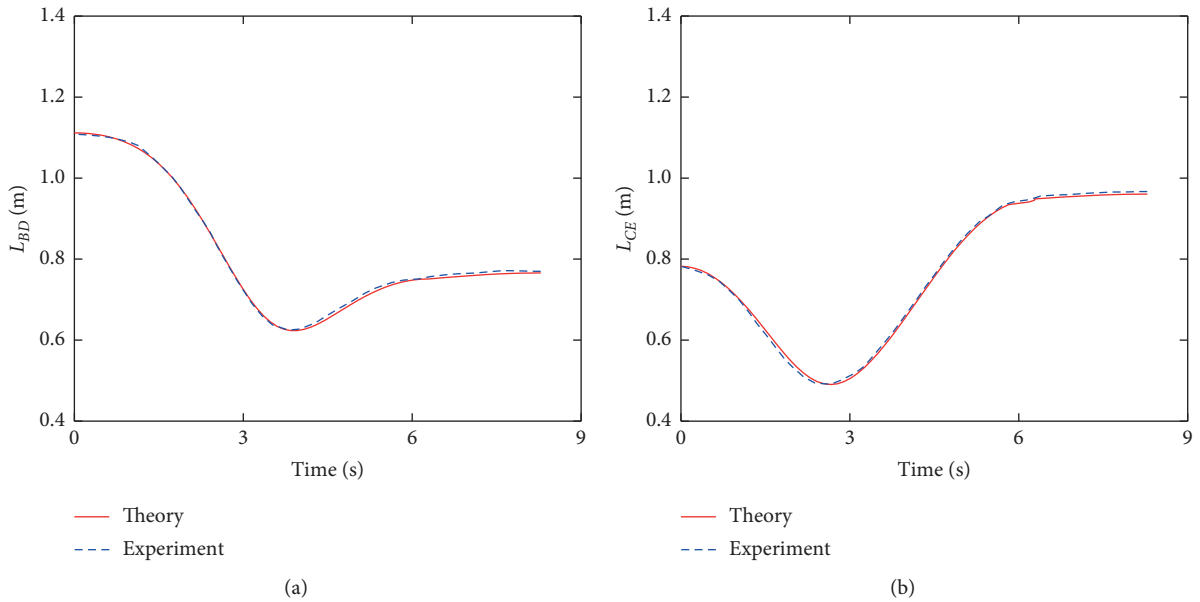

Figure 20: Comparisons of theory and experiment: (a) comparison of L_{BD}; (b) comparison of L_{CE}.

5. Conclusions

A novel CMRP is proposed, which has potential for agriculture. Aiming at the CMRP with four work patterns, its kinematics, including displacement, velocity, and acceleration, are analyzed in detail. Using the Newton–Euler method and Lagrange method, dynamics modeling of the CMRP with flexible patristic joint is established on the basis of kinematics. Then, based on the static balance analysis, the initial compression length of the spring with the elastic coefficient is

determined. And the numerical simulations containing kinematic models and dynamic models are performed using Matlab software and SolidWorks software, respectively. The comparisons, especially the error analysis of the actuation forces, show the validity of dynamic models. The internal forces acting on the revolute joints A, B, and C are also solved by means of separated model blocks, and the results are conducive to judge the joints stiffness. The contrast analyses of the displacements of the two hydraulic cylinders according to theoretical calculation and experimental verification are given, which is conducive to verify the correctness of the theoretical model.

The main contribution of this paper lies in the theoretical analysis of a novel CMRP, which lays a foundation for practical application with dynamic models taken into account. The research also shows that the pressure of the bottom of the rotary plough frame to the bottom of the groove can be adjusted to maintain the stability of the depth of the tillage. The metamorphic characteristics of the underactuated mechanism enhances the research application of the metamorphic mechanism. Therefore, the CMRP has potential application prospects. In our future work, field trail of this novel CMRP with outstanding performance will be performed.

Data Availability

All data generated or analyzed during this study are included in this published article, and other pieces of information are available from the corresponding author on reasonable request.

Conflicts of Interest

The authors declare that they have no conflicts of interest.

Acknowledgments

This work was supported by the National Natural Science Foundation of China (grant numbers 51275352 and 51475330), the Natural Science Foundation of Tianjin (grant numbers 17JCQNJC03900 and 18JCQNJC05300), the Tianjin Municipal Education Commission Research Program (grant number 2018KJ205), and the Program for Innovative Research Team in University of Tianjin (grant number TD13-5037).

References

[1] Y. Yin, S. Guo, Z. Meng, W. Qin, B. Li, and C. Luo, "Method and system of plowing depth online sensing for reversible plough," *IFAC-PapersOnLine*, vol. 51, no. 17, pp. 326–331, 2018.

[2] K. C. Mouli, S. Arunkumar, B. Satwik, S. B. Ram, J. R. Tej, and A. S. Chaitanya, "Design of reversible plough attachment," *Materials Today: Proceddings*, vol. 5, no. 11, pp. 23702–23709, 2018.

[3] L. Zhu, J.-R. Ge, X. Cheng et al., "Modeling of share/soil interaction of a horizontally reversible plow using computational fluid dynamics," *Journal of Terramechanics*, vol. 72, pp. 1–8, 2017.

[4] Y. Chen, F. Tian, Y. Yan et al., "Development overview and analysis of tillage machinery abroad," *Journal of Chinese Agricultural Mechanization*, vol. 39, no. 1, pp. 7–11, 2018.

[5] G. Gebresenbet, E. Zerbini, A. Astatke, and P. Kaumbutho, "Optimization of animal drawn tillage implement systems: part 2, development of a reversible plough and a ridger," *Journal of Agricultural Engineering Research*, vol. 67, no. 4, pp. 299–310, 1997.

[6] G. Moitzi, M. Haas, H. Wagentristl, J. Boxberger, and A. Gronauer, "Energy consumption in cultivating and ploughing with traction improvement system and consideration of the rear furrow wheel-load in ploughing," *Soil and Tillage Research*, vol. 134, pp. 56–60, 2013.

[7] M. Mahmoodi-Eshkaftaki, R. Ebrahimi, D. Ghanbarian, and E. Houshyar, "Geometric characterization of moldboard plough using coupled close photography and surface fitting model," *Soil and Tillage Research*, vol. 170, pp. 122–129, 2017.

[8] C. Galletti and P. Fanghella, "Single-loop kinematotropic mechanisms," *Mechanism and Machine Theory*, vol. 36, no. 6, pp. 743–761, 2001.

[9] J. S. Dai and J. Rees Jones, "Mobility in metamorphic mechanisms of foldable/erectable kinds," *Journal of Mechanical Design*, vol. 121, no. 3, pp. 375–382, 1999.

[10] J. Dai and Q. Zhang, "Metamorphic mechanisms and their configuration models," *Chinese Journal of Mechanical Engineering (English Edition)*, vol. 13, no. 3, pp. 212–218, 2000.

[11] W. Zhang, T. Wu, and X. Ding, "An optimization method for metamorphic mechanisms based on multidisciplinary design optimization," *Chinese Journal of Aeronautics*, vol. 27, no. 6, pp. 1612–1618, 2014.

[12] S. Li, H. Wang, Q. Meng, and J. S. Dai, "Task-based structure synthesis of source metamorphic mechanisms and constrained forms of metamorphic joints," *Mechanism and Machine Theory*, vol. 96, pp. 334–345, 2016.

[13] S. Li, H. Wang, X. Li, H. Yang, and J. Dai, "Task-orientated design method of practical constraint metamorphic mechanisms," *Journal of Mechanical Engineering*, vol. 54, no. 3, pp. 26–35, 2018.

[14] K. Xu, L. Li, S. Bai, Q. Yang, and X. Ding, "Design and analysis of a metamorphic mechanism cell for multistage orderly deployable/retractable mechanism," *Mechanism and Machine Theory*, vol. 111, pp. 85–98, 2017.

[15] X. Ma, K. Zhang, and J. S. Dai, "Novel spherical-planar and Bennett-spherical 6R metamorphic linkages with reconfigurable motion branches," *Mechanism and Machine Theory*, vol. 128, pp. 628–647, 2018.

[16] D. Zhang, Y. Xu, J. Yao, B. Hu, and Y. Zhao, "Kinematics, dynamics and stiffness analysis of a novel 3-DOF kinematically/actuation redundant planar parallel mechanism," *Mechanism and Machine Theory*, vol. 116, pp. 203–219, 2017.

[17] V. Venkatesan, J. K. Mohanta, S. K. Saha, and M. Santhakumar, "Dynamic modelling approaches for a 3-PPR planar parallel manipulator," in *International Conference on Advancements in Automation, Robotics and Sensing*, B. Vinod, R. Voyles, P. Vadakkepat, M. Sundaram, K. Sujatha, and J. Brislin, Eds., pp. 41–52, Springer, Singapore, 2016.

[18] S. M. Varedi, H. M. Daniali, M. Dardel, and A. Fathi, "Optimal dynamic design of a planar slider-crank mechanism with a joint clearance," *Mechanism and Machine Theory*, vol. 86, pp. 191–200, 2015.

[19] M. Sharifzadeh, A. Arian, A. Salimi, M. Tale Masouleh, and A. Kalhor, "An experimental study on the direct & indirect dynamic identification of an over-constrained 3-DOF

decoupled parallel mechanism," *Mechanism and Machine Theory*, vol. 116, pp. 178–202, 2017.

[20] G. Cheng and X. Shan, "Dynamics analysis of a parallel hip joint simulator with four degree of freedoms (3R1T)," *Nonlinear Dynamics*, vol. 70, no. 4, pp. 2475–2486, 2012.

[21] L. Dong, Y. Song, T. Sun, G. Dong, and B. Lian, "Dynamic modeling and performance analysis of a redundantly actuated 2-DOF parallel manipulator," in *International Conference on Intelligent Robotics and Applications*, H. Liu, N. Kubota, X. Zhu, R. Dillmann, and D. Zhou, Eds., pp. 408–419, Springer, Cham, Switzerland, 2015.

[22] A. Arian, B. Danaei, H. Abdi, and S. Nahavandi, "Kinematic and dynamic analysis of the Gantry-Tau, a 3-DoF translational parallel manipulator," *Applied Mathematical Modelling*, vol. 51, pp. 217–231, 2017.

[23] D. Gan, J. S. Dai, J. Dias, and L. Seneviratne, "Joint force decomposition and variation in unified inverse dynamics analysis of a metamorphic parallel mechanism," *Meccanica*, vol. 51, no. 7, pp. 1583–1593, 2016.

[24] G. Jin, X. Ding, and Q. Zhang, "Research on configuration-complete dynamics modeling and numerical simulation of metamorphic mechanism," *Acta Aeronautica Et Astronautica Sinica*, vol. 25, no. 4, pp. 401–405, 2004.

[25] S. H. Hu, H. G. Wang, X. L. Liu, and X. D. Zhang, "Research on configuration-complete dynamic modeling of metamorphic mechanism based on screw theory," *Advanced Materials Research*, vol. 655–657, pp. 531–536, 2013.

[26] L. Zhu, S.-S. Peng, Y.-Y. Qi et al., "An improved horizontally reversible plow design based on virtual assembly semantics and constraint," *Journal of Mechanical Science and Technology*, vol. 30, no. 1, pp. 257–266, 2016.

[27] Y. Li, H. Zhang, J. Han, and Q. Sun, "Distributed multi-agent optimization via event-triggered based continuous-time Newton–Raphson algorithm," *Neurocomputing*, vol. 275, pp. 1416–1425, 2018.

[28] S. Y. Gatilov, "Using low-rank approximation of the Jacobian matrix in the Newton–Raphson method to solve certain singular equations," *Journal of Computational and Applied Mathematics*, vol. 272, pp. 8–24, 2014.